



Deposition of Stellite 6 alloy on steel substrates using wire and arc additive manufacturing

Zidong Lin^{1,2} · Wei Ya^{1,3} · Vignesh Venkata Subramanian¹ · Constantinos Goulas^{1,2} · Benedetto di Castri¹ · Marcel J. M. Hermans² · Belavendram Pathiraj³

Received: 27 July 2020 / Accepted: 16 September 2020 / Published online: 28 September 2020
© Springer-Verlag London Ltd., part of Springer Nature 2020

Abstract

Stellite 6 is a cobalt-based superalloy which has a good wear and corrosion resistance and retains these properties at high temperatures. In this study, wire and arc additive manufacturing (WAAM based on the GMAW) was employed to deposit Stellite 6 wire on low alloy high strength steel (S355) and stainless steel (AISI 420) plates. One of the main interests of this study is to produce WAAM Stellite 6 deposits with quality comparable with laser deposition. The advantages of the WAAM process include the high deposition rate, high productivity, high material usage, and energy efficiency with low cost. However, superalloy deposition generally requires maintaining a low dilution level to avoid jeopardizing the integrity of the deposit. As a result, it is important to manage the excess heat input during the WAAM deposition process through a parametric optimization of WAAM deposition of Stellite 6 on S355 steel substrates. In this study, a WAAM process window is established to guide the process optimization. The optimization method used in this study has been applied in our previous laser cladding work. The generated process window also shows some correlations among the heat input, bead geometry, and dilution. The effects of heat input on the resulting microstructure, elemental distribution, and hardness were discussed. Dilution, microstructure, and hardness were considered for comparison from previous studies of laser cladding deposits. In addition, the obtained optimal conditions were adapted to apply WAAM deposition of Stellite 6 layers on AISI 420 stainless steel substrates. The XRD result shows that WAAM deposits contain Co-Cr-Fe solid solution (FCC), Cr₇C₃ and Cr₃C₂ carbides, and Co₄W₂C intermetallic compound. The results obtained through this study lay a foundation for future research on the wear properties of WAAM Stellite 6 deposits. This can contribute to further development of automated deposition of Stellite 6 using WAAM process for industrial applications.

Keywords Wire and arc additive manufacturing (WAAM) · Laser cladding · Stellite 6 · Steel · Materials processing

1 Introduction

Stellite 6 alloy is commonly used as a hardfacing alloy, which was developed in the early 1900s by Elwood Haynes [1]. It is a Co-based (Co-Cr-W-C) alloy with high hardness, good

corrosion, and wear resistance [2]. It was reported that different fractions of FCC and HCP crystal structures exist in Stellite 6 casting alloy. Pure cobalt has a hexagonal close-packed (HCP) crystal structure. The typical microstructure of the Stellite 6 alloy consists of α -Co (Co-rich matrix) dendrites with a face-centered cubic (FCC) crystal structure surrounded by a lamellar mixture of the Cr-rich phase and carbide phase resulting from the eutectic reaction into interdendritic phases during solidification [3]. Due to the addition of different elements in Stellite 6, the crystal structure (FCC or HCP) is affected. Specifically, the elements Ni, Fe, Mn, and C act as stabilizing elements of FCC structure, while W, Cr, Si, and Mo act as stabilizing elements of HCP structure [4].

In addition to the effects on crystal structure by the added elements, they contribute to the mechanical and physical properties of the Stellite 6. The presence of C decreases the solidification temperature and increases the solidification range

✉ Zidong Lin
a707169503@163.com

¹ Rotterdam Additive Manufacture Fieldlab (RAMLAB),
Scheepsbouwweg 8 F6, 3089JW Rotterdam, The Netherlands

² Department of Materials Science and Engineering, Delft University
of Technology, Mekelweg 2, 2628CD Delft, The Netherlands

³ Faculty of Engineering Technology, Department of Mechanics of
Solids, Surfaces & Systems (MS3), Chair of Laser Processing,
University of Twente, P.O. Box 217, 7500AE Enschede,
The Netherlands

according to the Co-C binary phase diagram [4]. Two main types of carbides can form as Cr-rich carbides (Cr_3C_2 , Cr_7C_3 , and Cr_{23}C_6) and refractory element-rich carbides (M_6C and MC) [5]. The presence of Cr provides oxidation and corrosion resistance. On one hand, Cr provides solute strengthening to the matrix. On the other hand, it also promotes the formation of Cr_7C_3 and Cr_{23}C_6 carbides to improve the hardness of the deposits. The addition of Mo influences the solidification behavior of cobalt-based alloys. This element has a dual function in the cobalt-based alloys. From the aspect of solid solution strengthening (below 8 wt.%), Kuzucu et al. [6] reported that the structure of Cr-rich carbide changes from M_7C_3 to M_{23}C_6 and its morphology from lamellar to granular shape in interdendritic regions with the addition of 6 wt.% Mo in Stellite 6 alloy. It can also form hard intermetallic compounds (such as Laves phases) with Co and other elements when its concentration is high (up to 28 wt.%) [7]. Tungsten W in Stellite 6 alloy normally contributes to the strength via precipitation hardening by forming WC carbide and intermetallic phases such as $\text{Co}_3(\text{W})$. The difference is that the Cr mainly provides resistance to corrosion and oxidation, while Mo and W improve wear properties.

Stellite 6 as a hardfacing material has been well studied and reported. It can provide sufficient hardness (380–490 HV) for wear and corrosion resistance, which has been applied in many harsh working environments [8–12]. As a valuable superalloy, Stellite 6 is normally deposited on the surface of large steel components to improve the surface performance through laser powder deposition [13]. Robotic laser deposition offers many attractive advantages including localized rapid heating and cooling, less distortion, excellent metallurgical bonding with minimum dilution (mixing) [14], and high level of automation [15]. Laser deposition of Stellite 6 has been studied by academics [16] and applied in the industrial applications [17]. The rapid cooling during laser deposition results in finer grain with hard phases, leading to a high hardness above 600 HV [18] and a low dilution level to ensure the integrity of the deposits. However, such high hardness will also increase the cracking tendency [19]. In addition, laser deposition is a high-cost process when compared with other arc-based deposition methods [20]. Therefore, a more economically viable processing method such as wire and arc additive manufacturing (WAAM) can be considered as alternatives on industrial scale as it offers low cost in investment and feedstock, high deposition rate, high material utilization efficiency, and high level of automation. In recent years, WAAM has been more and more successfully employed on various metallic materials for different applications such as nickel alloy [21], stainless steel [22], and Stellite 6 [23].

WAAM is an economic and efficient direct energy deposition (DED) method [24], which is a combination of an electric arc as a heat source and a consumable wire as feedstock. Either a 3D object or a 2D surface can be additively deposited.

Additionally, WAAM has been studied for applications in aerospace [25], automotive [26], marine [27], and construction sectors [28–30], due to its advantages over other powder-based direct energy deposition (DED) techniques [31]. However, not all arc heat sources of WAAM are suitable for industrial robotic production [32], depending on not only low costs but also product quality, materials, and high production rate [33]. For instance, gas tungsten arc welding (GTAW) is limited by its automation level, slower welding speed, and low deposition rate in the case of processing steel alloy [34, 35]. The plasma arc welding (PAW) requires high investments in equipment, has relatively low-energy efficiency, and needs highly skilled and specialized operators [36]. The bulky design of the welding torch also limits the movement freedom if mounted on a robotic arm [37]. Furthermore, laser welding or cladding, GTAW, and PAW normally require an independent feedstock unit. There are challenges in the synchronization between a heat source and feedstock system, which could affect the precision of the deposition.

Based on our previous knowledge of laser cladded Stellite 6 [14] and considering all the aspects mentioned above, the GMAW-based WAAM process is expected to be able to deposit the Stellite 6 on steel substrates with relatively low cost, high energy, and material efficiency with satisfactory material properties and has the potential to achieve the high level of automation for industrial applications. To the best knowledge of the authors, the sensor-based robot arc welding system in the past was not well developed [38]; only a limited amount of literatures have reported the development of an automated cladding process using WAAM. Therefore, this study mainly focuses on the fundamental of Stellite 6 deposition on the steel substrates using the GMAW-based WAAM. To evaluate the optimization method used, this study will also focus on the process optimization and analyzing the resulting dilution, microstructure, elemental distribution, and hardness. These values are to be used as criteria during the optimization process, as proper bead characteristics, and the hardness indicating the mechanical properties is important to provide navigation to further achieve high-quality layer deposition. These research results will lay a strong foundation for automated WAAM Stellite 6 deposition for future industrial applications.

2 Experimental details

2.1 Materials used

Steel substrate plates used in this study have the size of $250 \times 60 \times 10 \text{ mm}^3$ (S355 steel and AISI 420 stainless steel). A Stellite 6 metal-cored wire (WEARTECH WT-6 GMAW-C produced by Lincoln Electric) with a diameter of 1.2 mm was used as the filler wire. The chemical composition of materials used in this work is listed in Table 1 and Table 2. For

Table 1 Chemical composition of steel plates (wt.%)

Materials	C	Si	Mn	P	Cu	Fe	Cr
S355 steel plate	0.2	0.55	1.6	0.025	0.55	Bal.	/
AISI 420 steel plate	< 0.15	< 0.55	< 1.0	< 0.04	/	Bal.	12–14

comparison, the typical chemical composition of Stellite 6 powder from manufacturer is also listed in Table 2. The S355 steel was used as a substrate for process optimization as it is more cost-saving than the AISI 420 steel. The optimal condition was applied to AISI 420 steel substrates, which is commonly laser deposited with Stellite 6 against erosion and wear [39, 40].

2.2 Experimental setup

The schematic of experimental setup is shown in Fig. 1a. WAAM experiments were performed using active wire production (AWP, MAG welding with Alumaxx as shielding gas) with the Panasonic TM-1400WG3-AWP 6-axis welding robot and an additional 2-axis workpiece manipulator (type YA-1RJC62) integrated by Valk Welding. The schematic drawing of the deposition tool path is shown in Fig. 1b. The deposition conditions used are listed in Table 3. Before deposition started, the top surface of the substrate was adjusted to the flat position and cleaned using acetone ((CH₃)₂CO) solution to remove all surface contaminants.

2.3 Ramping experiments and bead characteristic

To investigate the effect of different processing parameters on the characteristics of the deposited Stellite 6, ramping deposition strategies were adopted in this study. It is a cost-effective and time-saving approach, which used different processing parameters on one bead but at different length sections to avoid redundant experiments. It is also the technique used in a previous laser powder material deposition study of some of the authors, where similar processing windows were established [41]. The ramping experiment is schematically shown in Fig. 2. The obtained process window will be compared with the laser powder deposition process windows

Table 2 Chemical composition of Stellite 6 feedstock (wt.%)

Materials	C	Si	Mn	W	Cr	Fe	Mo	Ni	Co
Stellite 6 metal-cored wire (WEARTECH WT-6 GMAW-C AWS A5.21 ERCCoCr-A)	1.2	0.5	0.8	4.1	28.2	3.9	0.1	0.3	Bal.
Stellite 6 powder ((SF)A 5.21 ERCoCr-A)	1.2	< 2	/	4–5	30	< 3	< 1	< 3	Bal.

based on the effective energy input. This will be further discussed in Section 3.1.

Figure 3 shows a cross section and schematic of a deposited bead characteristics including width (W_b), height (H_b), melt depth (d_m), and heat affected zone (HAZ). Figure 3a shows a schematic and Fig. 3b shows cross section of an actual deposited bead. The bead width over bead height is defined as the aspect ratio ($AR = W_b/H_b$) [42]. The geometrical dilution is defined as the ratio of melt depth over the sum of the melt depth and bead height ($D_d = 100\% \times d_m/(d_m + H_b)$). The elemental dilution is represented by the percentage of Fe content in “deposited bead” region. The heat penetration depth is defined as a sum of melt depth + HAZ depth.

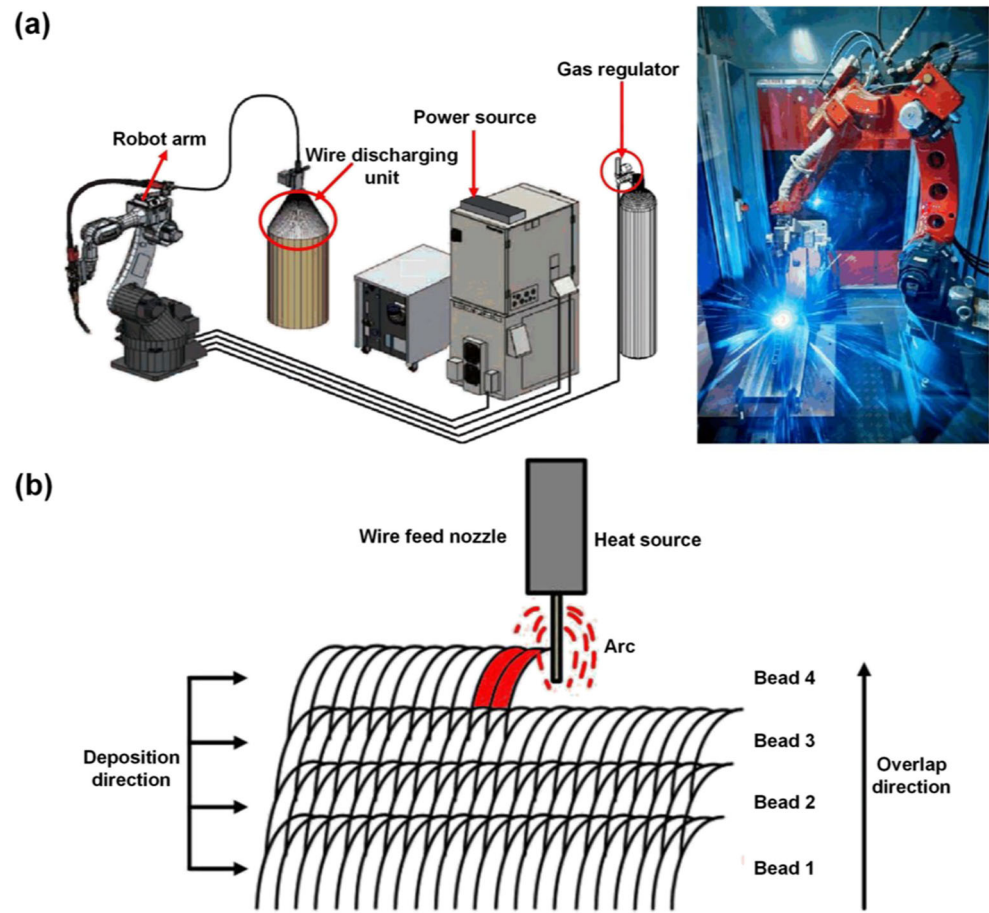
2.4 Overlap ratio experiments

In addition, experiments were performed by overlapping beads through lateral displacement of the robot arm (d_r) to determine the optimal overlap ratio ($OR = 100\% \times (W_b - d_r)/W_b$). Overlap ratio values were determined based on the dimension of the bead, which will avoid inter-run porosity (too small OR) at the weld toe and deep valley (too big OR) on the surface of laid beads. The overlapping deposition in this study consisted of seven overlapped beads. The length of each bead is 200 mm. The deposition process is continuous without inter-pass cooling after depositing each bead. After the deposition, the deposited layer was naturally air cooled to room temperature. Samples were cut and prepared according to standard metallurgical procedure for further analyses.

2.5 Metallurgical analysis and microhardness measurements

For a better understanding of the material responses to the WAAM deposition process, the cross section of the as-deposited Stellite 6 samples were prepared for metallurgical investigation. Two-step etching procedures were carried out. A 2% Nital (98% ethanol and 2% HNO₃) was used to reveal the microstructure of the substrate (S355 and AISI 420), and an Aqua regia (25% HCl and 75% HNO₃) solution was used to reveal the microstructure of the deposited Stellite 6. The etched cross sections were observed using a KEYENCE VHX-5000 optical microscope (OM) for weld geometry characterization. To further qualitatively evaluate the resulting

Fig. 1 **a** The experimental setup.
b Schematic drawing of deposition tool path



microstructure of WAAM Stellite 6 on the steel substrates, X-ray diffraction (XRD) analyses were performed. A Bruker D8 Advanced diffractometer with Bragg-Brentano geometry, equipped with a graphite monochromator and Vantec position-sensitive detector, was used. Samples were scanned using Co K α radiation (45 kV 35 mA) with a divergence slit 6A16 V20 and no scatter slit. The coupled θ – 2θ scan was performed using a 2θ step size of 0.035 degree, and counting time per step was 4 s. Similar phases were identified in both

cases (Stellite 6 + S355 and Stellite 6 + AISI 420). The obtained X-ray patterns were analyzed using the Bruker software DiffracSuite.EVA vs 5.0. The JEOL JSM-5600 field emission scanning electron microscope (FESEM) was used to reveal the microstructure with a high resolution. The phase characterization and elemental distribution were examined through energy dispersive spectroscopy (EDS). The hardness of the cross section was measured using the Struers DuraScan-70 hardness test machine. The Vickers pyramid hardness was tested using a 0.2 kgf and a loading time of 15 s.

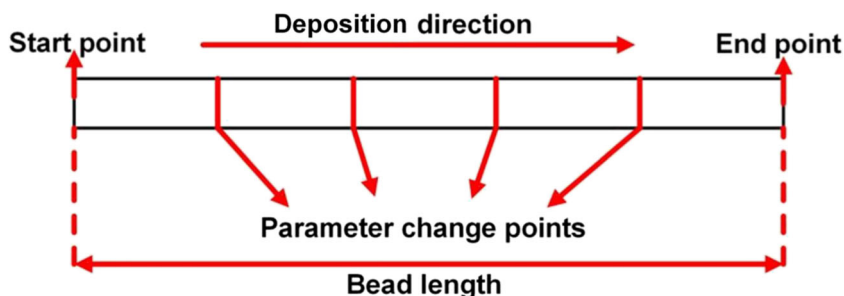
Table 3 The deposition parameters used

Current (I)	180 (A)
Voltage (U)	10.2–29.2 (V)
Wire feed speed (WFS)	0.5–5 (m min^{-1})
Deposition speed (v)	1 and 1.5 (m min^{-1})
Contact tip-to-work distance (CTWD)	0.001 (m)
Shielding gas flow rate (30% He + 70% Ar)	18 (L min^{-1})
Polarity	Direct current, reversed polarity
Stick out length	0.015 (m)

3 Results and discussion

In the direct energy deposition (DED) process, it is essential to understand how the material responds to the supplied energy. The measured responses in our case were the bead geometry, dilution, microstructure, elemental distribution, and hardness, which can help to determine the optimal deposition conditions [43, 44]. The effect of different heat input levels (combinations of different deposition parameters) on the bead characteristic was evaluated through the ramping tests.

Fig. 2 Schematic of ramping deposition



3.1 The bead geometry and process window

Figure 4 shows the Stellite 6 bead deposited at various process conditions using the ramping approach. The discontinuous and unstable beads, due to the low heat input, are marked with a yellow dashed line. As the heat input increases, it is easier to deposit continuous bead as the energy is sufficient to melt the electrode filler metal and encourage the spreading of the melt due to the reduced surface tension. The continuously deposited beads are marked with the blue dashed line in Fig. 4. Narrow bead shape leads to a small aspect ratio. More energy is needed to obtain a better bead shape, which will be suitable for overlapped deposition used for 3D printing/additive manufacturing. The further increasing heat input helps melt pool spreading, resulting in wider bead and hence a larger aspect ratio. Samples shown in Fig. 4 were subsequently cut, and cross sections were prepared for further analyses.

A process window is generated based on the cross sections obtained from Fig. 4 as shown in Fig. 5. The minimum heat input during WAAM depositing of Stellite 6 was found to be around 55 J mm^{-1} in this study. To a certain degree, this finding can be regarded as a basic reference for the future parameters optimization of depositing Stellite 6 on steel substrates. The aspect ratio varies from 2.25 to 4.02 at different heat input levels. Dilution can be achieved below 5% to reach the level with laser deposition [45]. As the heat input increased, both aspect ratio and dilution increased. However,

excessive heat input can lead to an excessive dilution [46] and jeopardize the integrity of the deposited material, which often reflects on the hardness value. Therefore, bead geometry, dilution, and hardness need to be considered during parametric optimization, where the lower dilution will have a minimum influence on the deposited material properties. A larger aspect ratio [47] will be preferable for overlapped deposition.

Schneider [48] has reported that 15% of the dilution for laser depositing Stellite 6 on steel substrate is necessary to be effective in achieving clad layers with good hardness and bonding. It was also reported that the hardness can reduce to around $500 \text{ HV}_{0.2}$ [14] when the dilution is above 28% during laser cladding. According to the data shown in Fig. 5, to ensure the material properties with good bead geometry, the aspect ratio is appreciate to be larger than 3, and the dilution level can be kept between 10 and 20%, which can be used as primary criteria for the process optimization in this study. Therefore, the conditions A, B, C, D, and E (in Table 4) are identified as candidates for further study in the overlapped deposition experiments. Comparing results from these conditions with our previous results of laser cladding [41], similar graphs Fig. 6a and b can be plotted using the supplied laser energy and arc energy.

It is interesting to notice in Fig. 6a and b that the material has similar responses to the supplied energy as both the heat penetration depth and aspect ratio of the deposits increase with the increased energy in general. Specifically, the trend of

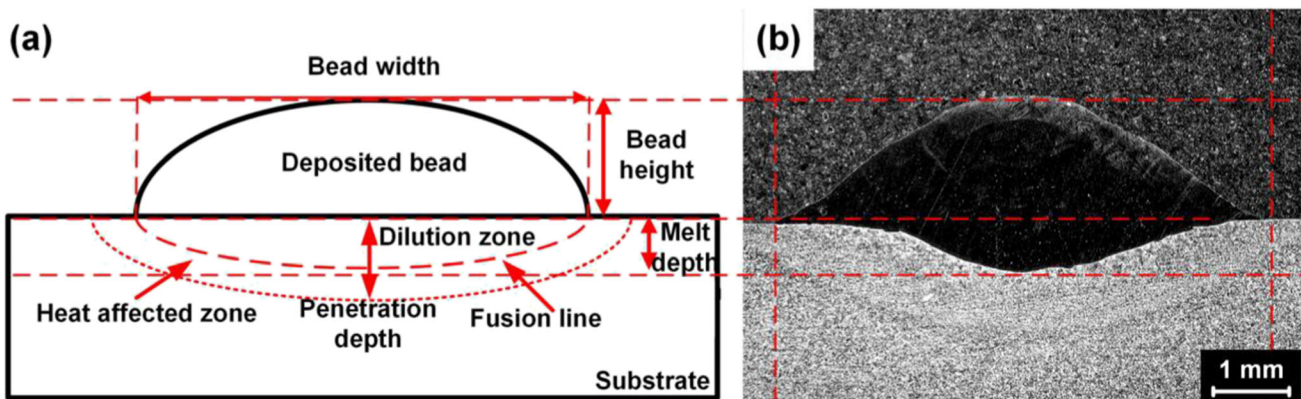
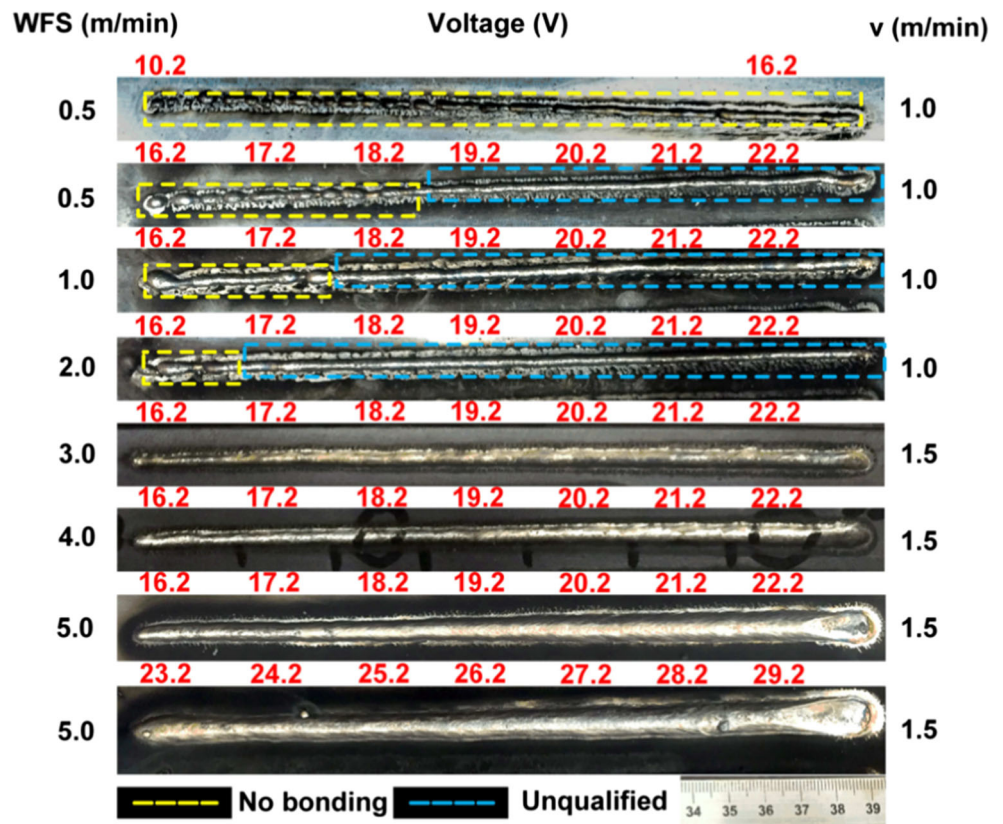


Fig. 3 Stellite cross section: (a) schematic drawing and (b) as deposited Stellite 6

Fig. 4 The overview of the ramped WAAM deposits



aspect ratio (blue dashed lines) for laser and WAAM processes contains two stages. The steep slope in the early stage indicates a limited wetting and bonding due to insufficient energy. When the energy reached a critical limit, the melt spreads gradually, which is indicated by the gentle slope in the second stage.

It is well known that the way of powder feeding is different between co-axial and off-axial laser cladding. In this study, total effective energy absorbed from laser beam is assumed to be same for off-axial and co-axial feeding due to no significant loss. However, compared with co-axial feeding, no powder cloud formed for off-axial powder feeding, which means the

Fig. 5 The WAAM process window for Stellite 6 deposition

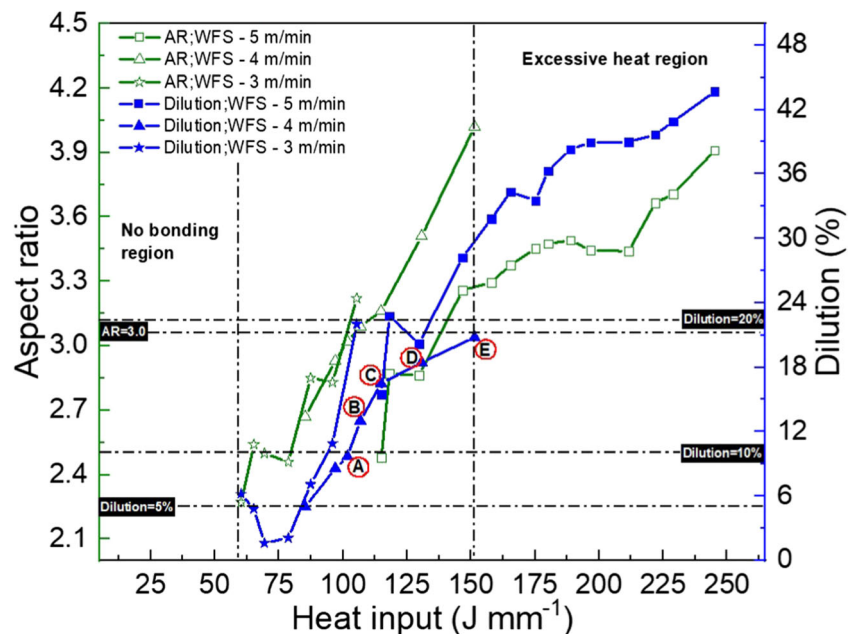


Table 4 The candidate WAAM process conditions used in this study

	Condition A	Condition B	Condition C	Condition D	Condition E
Energy input (J mm ⁻¹)	101	107	115	127	152
Aspect ratio	2.8	3	3.23	3.51	4.02
Dilution	9.7	13	16.5	18.1	20.8

interaction time between powder particles and laser beam is small. In this case, more energy is absorbed by the substrate and lesser by the powder stream compared with the co-axial feeding. This results in a larger heat penetration depth by increasing HAZ depth as shown in Fig. 6a. Considering the energy efficiency of the YAG laser (50% [49]) and consumable electrode arc welding (84% [50]), Fig. 6c is plotted to compare the laser and WAAM processes. It shows that the onset of bead spreading is in the similar energy region between 80 to 90 J mm⁻¹. Afterward, the aspect ratio shows a gradual linear increase as the energy input increases. The difference is that the spreading in WAAM is less than the co-axial and off-axial laser cladding cases, where powder was used during laser deposition.

The condition D, as shown in Fig. 5 and Fig. 6, is selected as it has a relatively large aspect ratio for WAAM process. For comparison, the conditions A and E were also studied as they represent different dilution levels. Hence, hardness measurements were performed on the single beads deposited using conditions A, D, and E on S355 steel substrate. The average hardness measured was 581 ± 15.8 HV_{0.2} (condition A, dilution, 9.7%), 553 ± 10.5 HV_{0.2} (condition D, dilution, 18.1%), and 506 ± 9.7 HV_{0.2} (condition E, dilution, 20.8%). The average hardness of laser clad samples measured at dilution around 15% was 530 ± 15 HV_{0.2} [13].

The SEM micrographs (Fig. 7a, b, and c) are obtained on the WAAM samples produced using conditions A, D, and E. They show that the average primary dendrite size increases

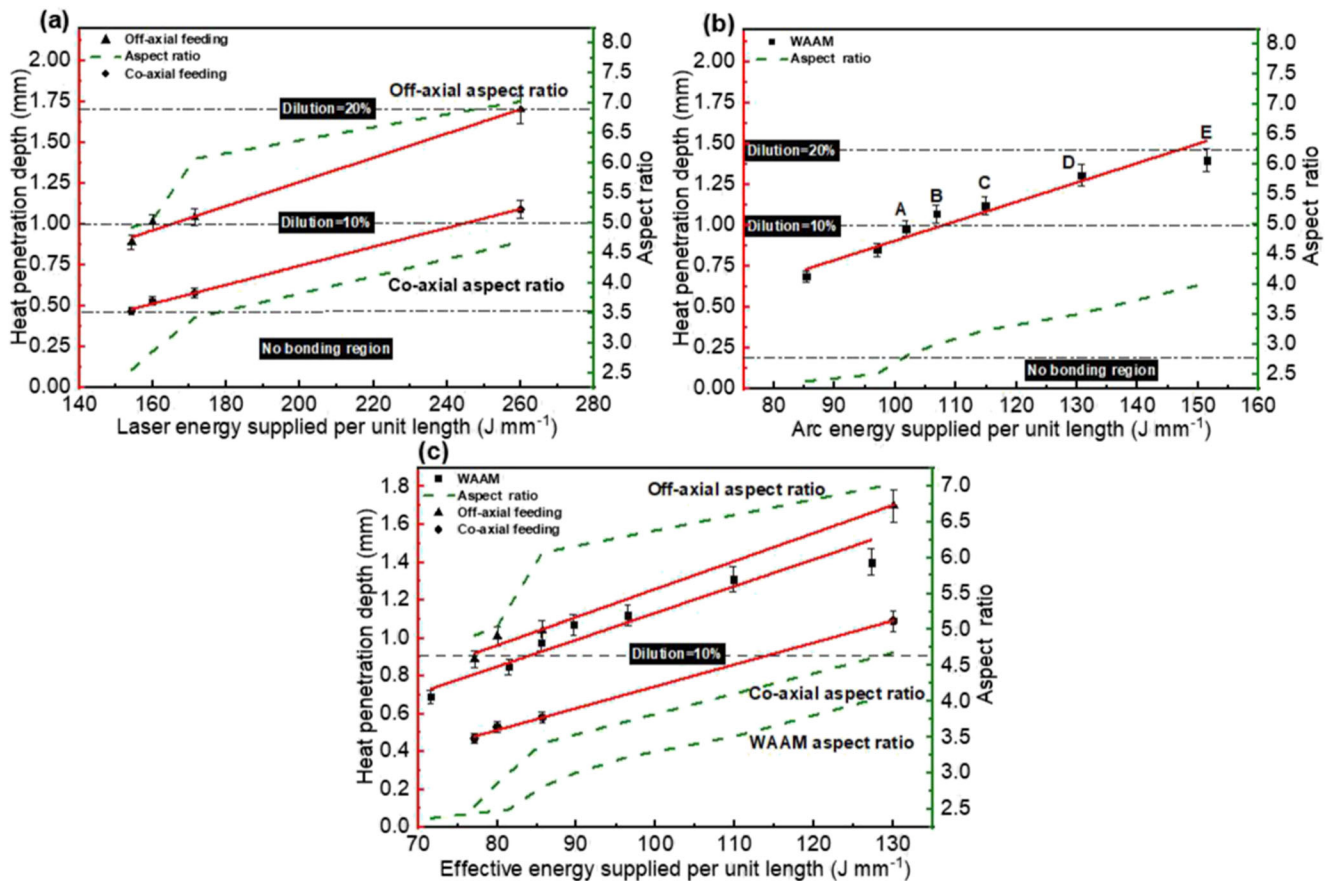


Fig. 6 a Changes in laser clad aspect ratio (dashed line) and heat penetration depth (solid line) with laser energy [41]. b Changes in WAAM bead aspect ratio (dashed line) and heat penetration depth (solid line) with arc energy. c Comparing laser and WAAM heat penetration depth and the aspect ratio

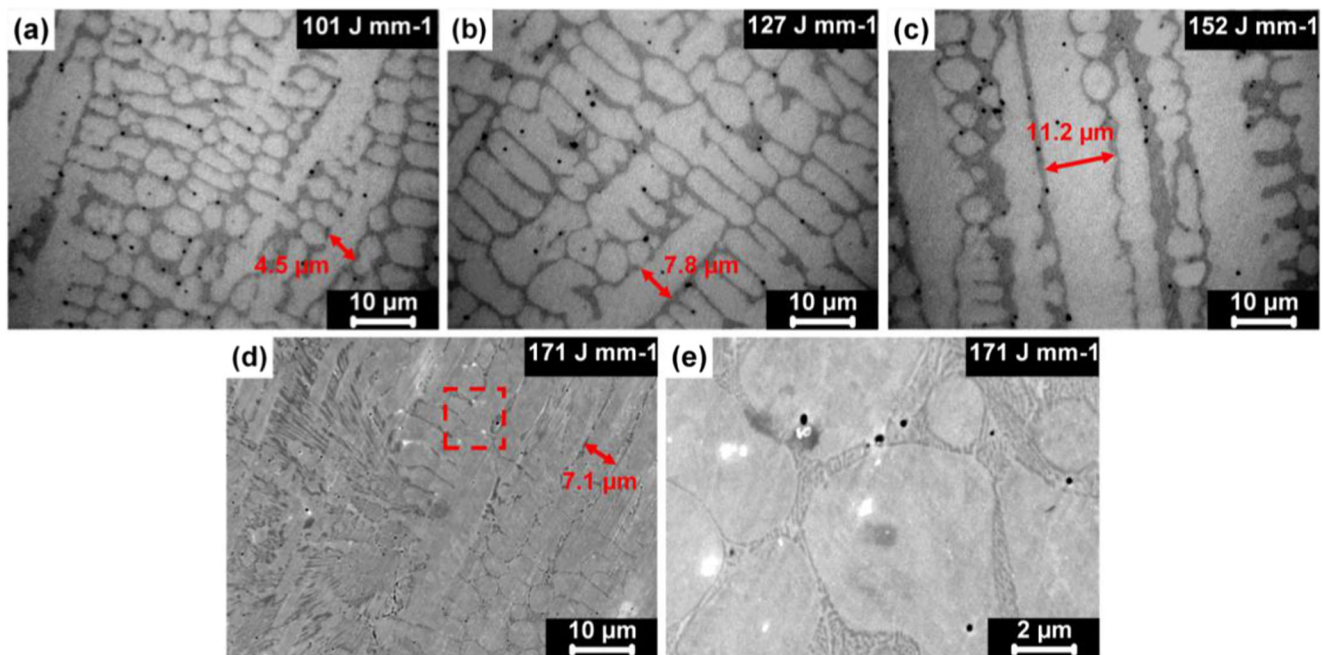


Fig. 7 The microstructure under different heat input, (a) condition A, (b) condition D, (c) condition E, (d) laser clad around 15% geometrical dilution, (e) higher magnification of the marked region in (d)

with the increased heat input, which is also observed and reported by other researchers [51, 52]. The size of the primary solidified dendrites increases with the increased heat input, indicating that the cooling rate decreased. This can contribute to a hardness reduction together with the Fe dilution from the substrate, which has been reported in the literature [53, 54]. SEM micrographs (Fig. 7d and e) of the laser clad with 15% dilution compares well with WAAM samples produced using condition D. Carbides formation at both eutectic region and the primary dendrites is noticed. The formed carbides appear to be smaller in laser clad samples, which is maybe due to the higher cooling rate observed for laser cladding. From the above-mentioned analysis, it can be concluded that WAAM is capable to deposit Stellite 6 on steel substrate with satisfactory material properties, similar to the ones obtained by laser cladding.

3.2 Microstructure and elemental distribution

With processing condition D, the optical micrographs in Fig. 8 and Fig. 9 show that the similar microstructures are obtained when WAAM depositing on both S355 and AISI 420 stainless steels. The observed microstructural variations (Fig. 8(a)–(e) and Fig. 9a–e) from the fusion line to the top of the beads (location D to A) are due to the cooling rate differences at different locations during solidification. The temperature gradient (G) over the moving solidification interface (solid-liquid) moving velocity is much larger at the fusion line than in other positions of the melt pool [55]. It is followed by the cellular (Fig. 8(e)) and columnar grain growth toward the

center of the bead where the primary grain solidifies with a slower cooling rate. Small equiaxial grains (Fig. 8(b) and Fig. 9b) are observed in edge locations of beads (location A) where the conduction and convection cooling with ambient room environment exists. This results in finer grain as its cooling rate is relatively higher than at the center of the bead. The observed microstructure similarity suggests that the adopted process optimization technique can be applied to different steel substrates.

In general, the observed microstructures in the Stellite 6 deposits belong to a hypo-eutectic structure consisting of the primary dendritic cobalt solid solution and an eutectic mixture of Co-Cr solid solution and Cr-rich carbides. The high-resolution SEM micrographs of WAAM deposited Stellite 6 are shown in Fig. 9a–d. The lamellar interdendrite is composed of Co-rich solid solution and eutectic carbides as indicated in Fig. 9d. The eutectic carbides exist as a network formed inside the interdendrite and mixed with the Co-rich phase (Fig. 9e). The dendritic region is expected to be richer in Co, and the interdendritic region is expected to be richer in Cr, W, C, and Si elements. Cr, W, C, and Si elements in the interdendritic regions can contribute to the formation of hard carbides such as Cr_{23}C_6 and Cr_7C_3 [5]. However, as pointed out by Houdkov et al. [56], the hard carbide contributions to wear mechanism is not fully understood in the scientific community. Hence, the wear properties of the WAAM deposited Stellite 6 needs to be further investigated separately.

For comparison, Fig. 10(a) is presented as the cross section of the WAAM deposited Stellite 6 on the AISI 420 steel

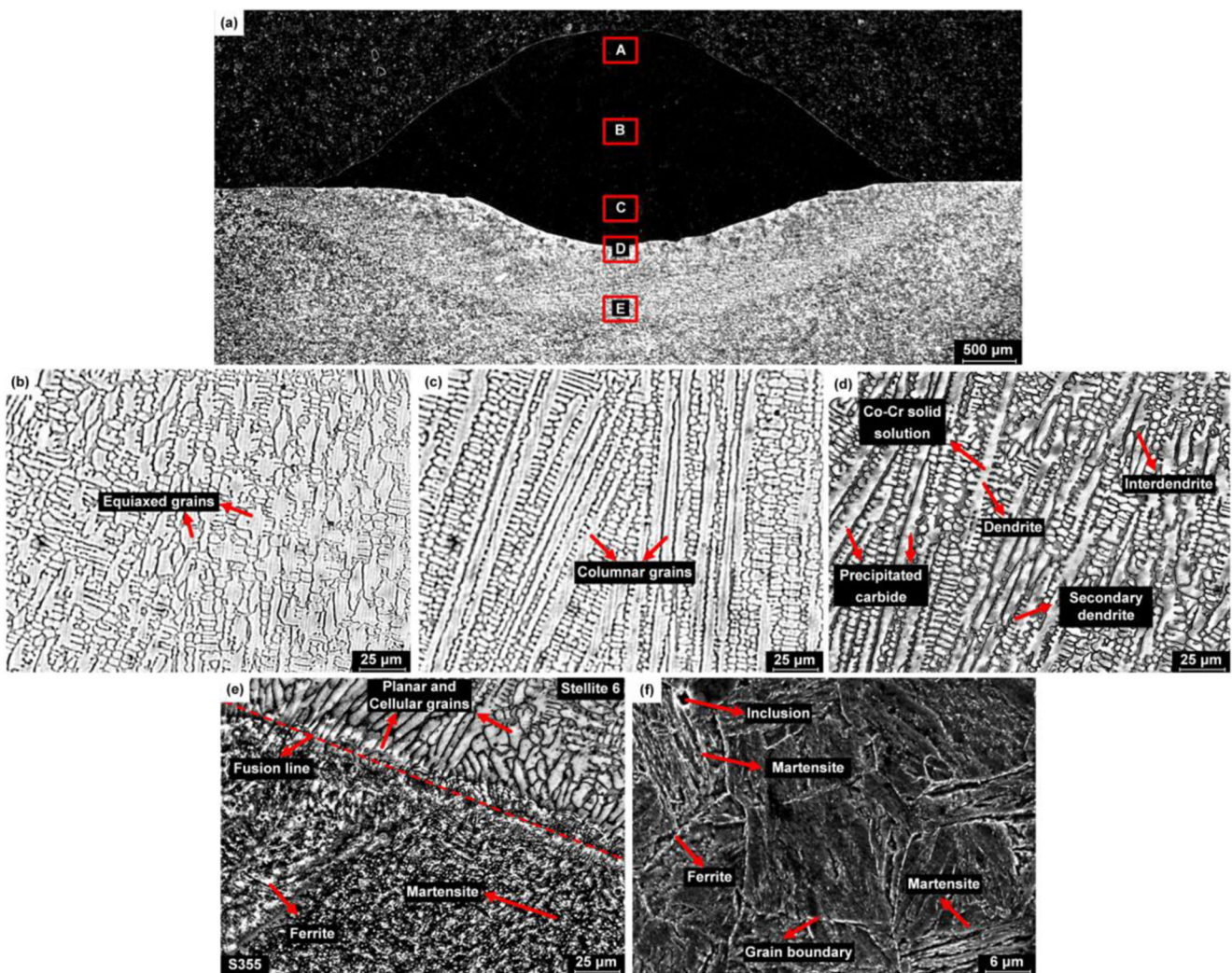


Fig. 8 Cross section of Stellite deposits on the S355 using condition D, (a) overview, (b) top of the bead (location A), (c) center of the bead (location B), (d) within the bead close to fusion line (location C), (e) around the fusion line (location D), (f) in the substrate (location E)

substrate using the condition D. From the fusion line to the top of the deposit (Fig. 10(b)–(e)), similar microstructure behavior during solidification is observed as shown in Fig. 8. Hence, it is expected that similar material properties are to be obtained when condition D is used to WAAM depositing Stellite 6 on S355 and AISI 420 steel substrates.

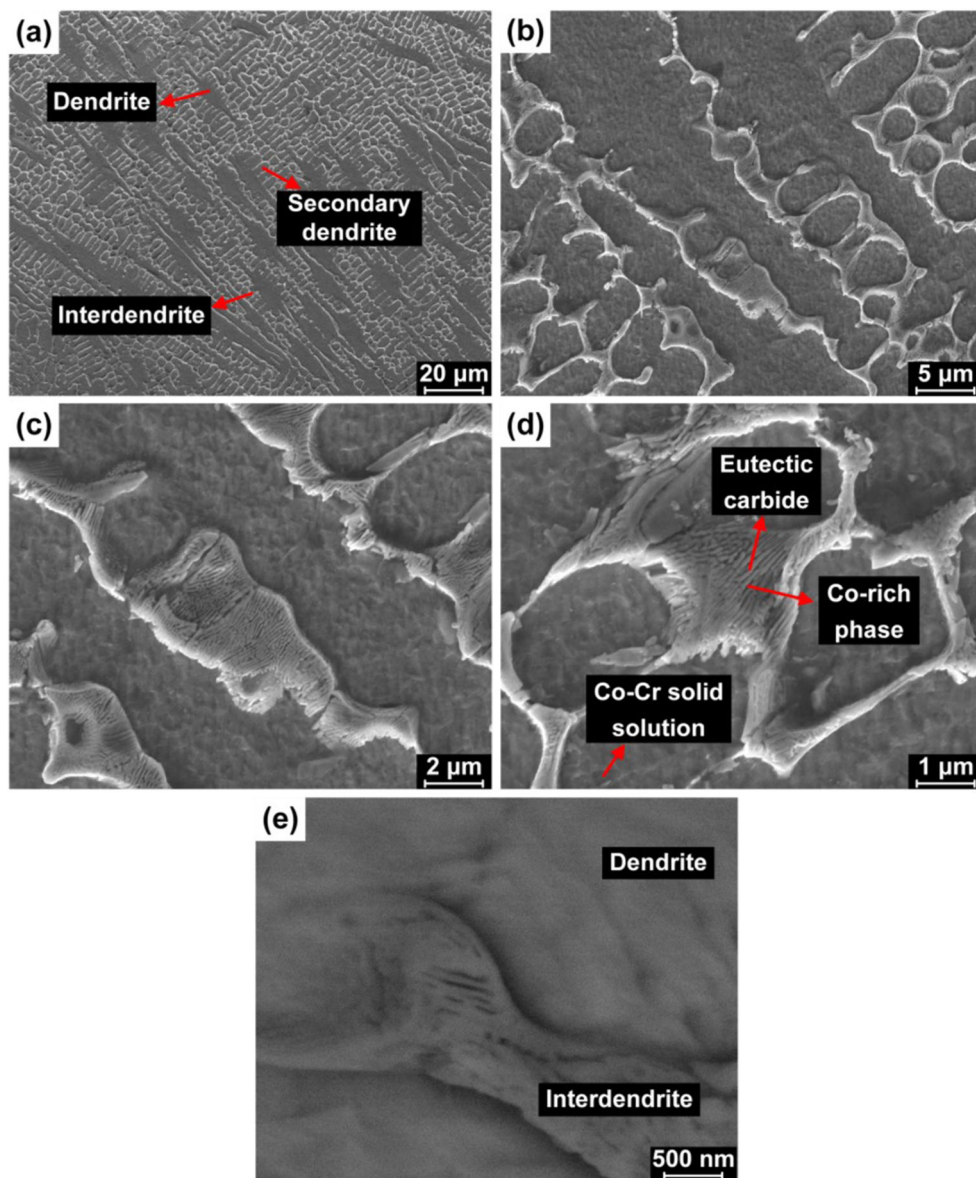
As reported by Ya et al. [14], the Fe dilution in the Stellite 6 can lead to the hardness reduction. The increase in the Fe content is suspected to be the reason for the hardness reduction as Fe promotes Co phase transition from HCP to FCC. The experimental results obtained by Xu et al. [57] show that a Fe dilution of 46% reduces the hardness to around 400 HV_{0.2}. In our cases, the elemental distribution in the samples produced with conditions A, D, and E on S355 steel substrate and AISI 420 stainless steel substrate was examined through the line scanning along the center of the bead from substrate to the deposit top using energy dispersive spectroscopy (EDS) as shown in Fig. 11. It shows a relatively uniform elemental

distribution, which indicates that uniform Stellite 6 layer with overlapping beads can be WAAM deposited.

3.3 WAAM deposition of overlapped beads - single layer

In practice, a surface is continuously clad by overlapping several beads (then called as a clad layer), which can be scaled up for applications. Hence, several overlap ratio values (30–60%) were investigated using conditions A, D, and E on both S355 and AISI 420 substrates. The deposited layers under different conditions are presented in Fig. 12a–h. Based on the surface waviness (peak-to-valley distance), dilution level (geometrical), and considering the elemental distribution, the 42% overlap ratio with condition D on S355 steel (Fig. 12c and d) is identified to be optimal, when considering the balance between waviness and satisfactory dilution. These results are summarized in Table 4. The surface waviness was

Fig. 9 SEM micrograph of WAAM deposited Stellite 6: (a) overview of Stellite 6 deposits, (b) primary and secondary dendrites, (c) lamellar interdendrite and dendrite, (d) eutectic carbide, (e) dendrite and interdendrite morphology at high resolution



measured using optical microscope, and minimum/maximum dilution is calculated using geometrical definition [58].

Therefore, both Stellite 6 single bead and overlapped beads were deposited on the AISI 420 steel substrates using condition D. The average hardness of the obtained single bead was measured to be $547 \text{ HV}_{0.2} \pm 7.4 \text{ HV}_{0.2}$. The obtained waviness and dilution were comparable with the results of WAAM deposited Stellite 6 on S355 steel substrates (Table 4).

It is interesting to observe from Fig. 12 that with the increased heat input, the surface waviness reduces due to the ability of the molten metal to provide sufficient energy to support its flow. With the heat accumulation in the substrate, the dilution was expected to increase as deposition progresses and becomes stable eventually when a thermal balance is reached [59]. However, during WAAM overlapped bead

deposition, the supplied arc energy is partially used to melt previously laid layer, resulting in less dilution as shown in Fig. 12b, d, f, and h. It is important that the dilution can be kept at a satisfactory level (smaller than 28% as mentioned earlier) to maintain the material properties. The maximum geometrical dilution (represented by the largest substrate melting by the bead) and the minimum geometrical dilution (represented by the smallest substrate melting by the bead) of the layer shown in Table 5 agree with the single bead data based process window shown in Fig. 5.

EDS scanning along the transverse cross section of the WAAM deposited Stellite 6 layer on S355 and AISI 420 steel substrates was performed, and obtained results are shown in Fig. 13. Various locations within the layer were examined. The scanning paths are selected in the transition zone between

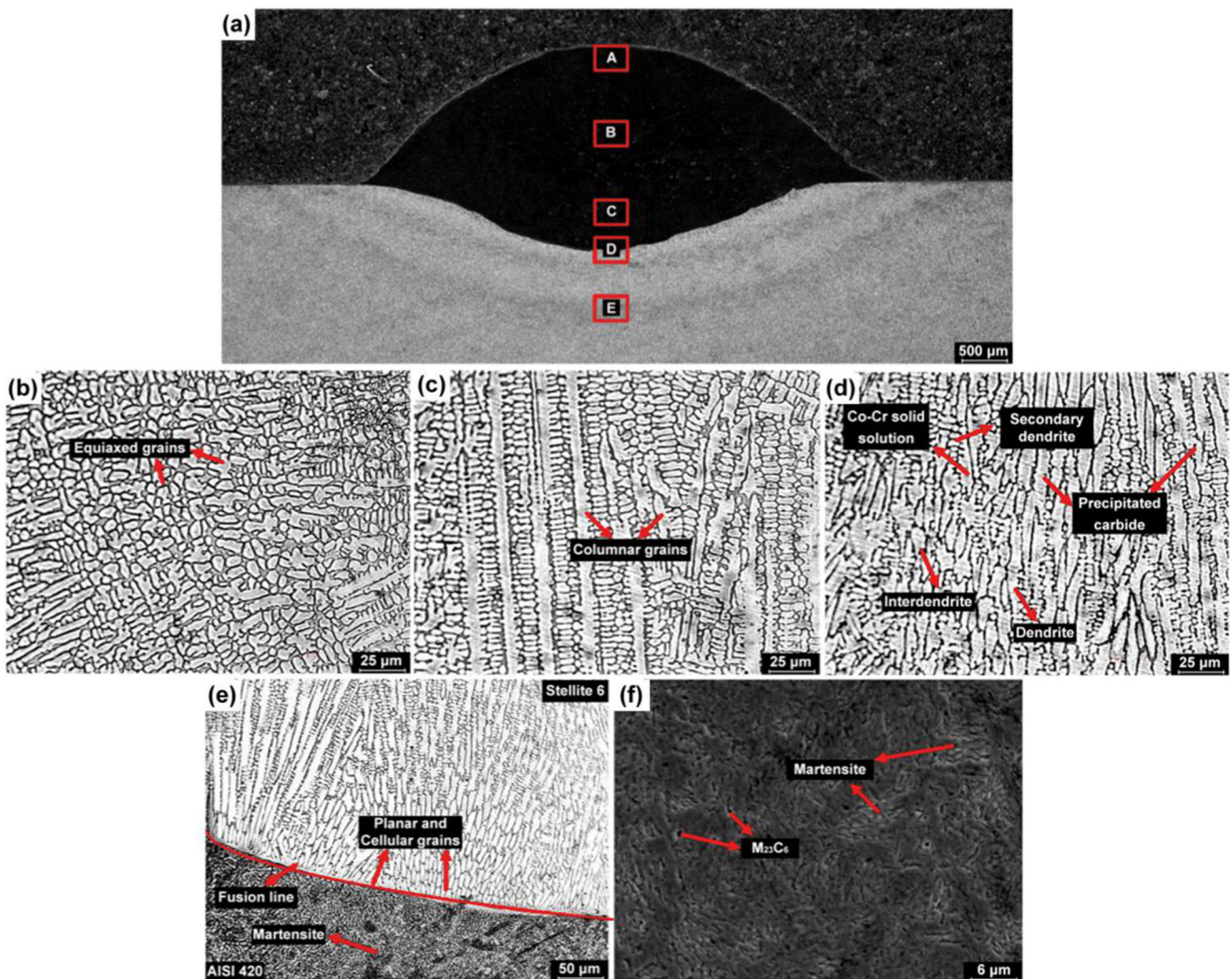


Fig. 10 Cross section of Stellite 6 deposits on the AISI 420 steel substrate using condition D: (a) overview, (b) top of the bead (location A), (c) center of the bead (location B), (d) within the bead close to fusion line (location C), (e) around the fusion line (location D), (f) in the substrate (location E)

the adjacent beads so that any variation of the element content can be checked directly. It can be seen from Fig. 13 that Fe, Cr, Co, and W elements are distributed fairly uniformly, with fluctuations of 4.05%, 2.69%, 4.88%, and 5.85%, respectively. This result has a good correlation with the uniform microhardness observed and presented in Fig. 14. The average measured microhardness of the deposited single bead (dashed line) is also plotted in Fig. 14a together with the hardness profile of the deposited overlapped layers produced under different WAAM conditions. It is noticed that the hardness of overlapped layers decreased slightly comparing with single bead average hardness. The relatively uniform hardness distribution in the longitudinal direction (Fig. 14b) indicates that the microstructure under overlapping condition is expected to be uniform within each deposited beads.

The cumulative heat input introduced by the thermal cycles can promote the Fe dilution. However, as part of

the arc energy is used to re-melt previously laid bead, this can lead to a melt depth reduction and a lower dilution. Eventually, a thermal balance can be reached, which can maintain the dilution level between 10 and 20%. This indicates that the effect of thermal cycles on elemental distribution is marginal when WAAM deposition of Stellite 6 on steel substrates is done.

3.4 XRD phase identification of WAAM Stellite 6 on steel substrates

The XRD results (Fig. 15) show that the FCC structure is a Co-rich solid solution matrix with elements such as Cr and Fe dissolved inside. The Cr_7C_3 and Cr_3C_2 were identified as the carbides present in the deposits. The intermetallic compound was identified as $\text{Co}_4\text{W}_2\text{C}$. The Cr_{23}C_6 carbide was not found in the WAAM deposited Stellite 6

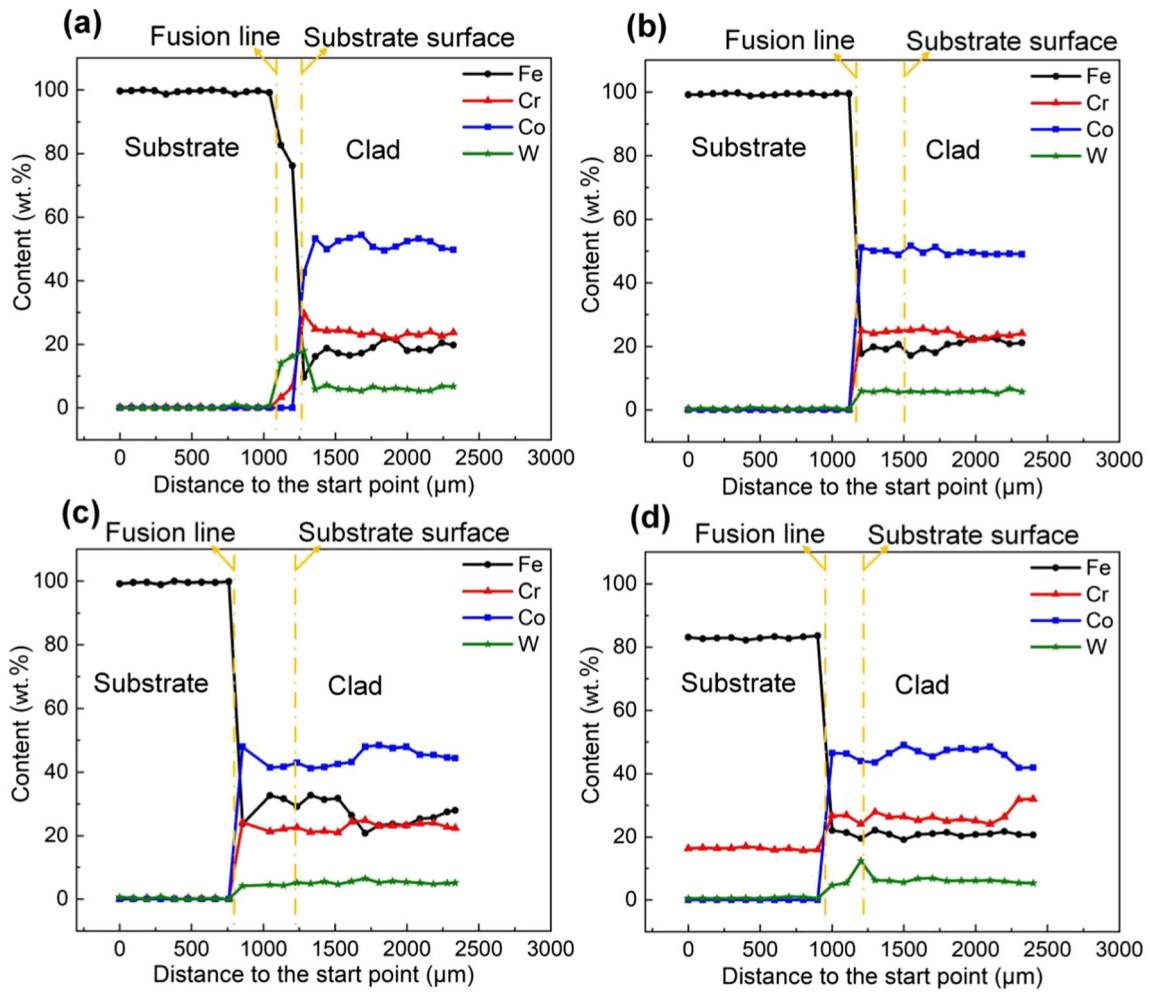


Fig. 11. Elemental distribution measured using EDS: (a) condition A (Stellite 6 + S355), (b) condition D (Stellite 6 + S355), (c) condition E (Stellite 6 + S355), (d) condition D (Stellite 6 + AISI 420)

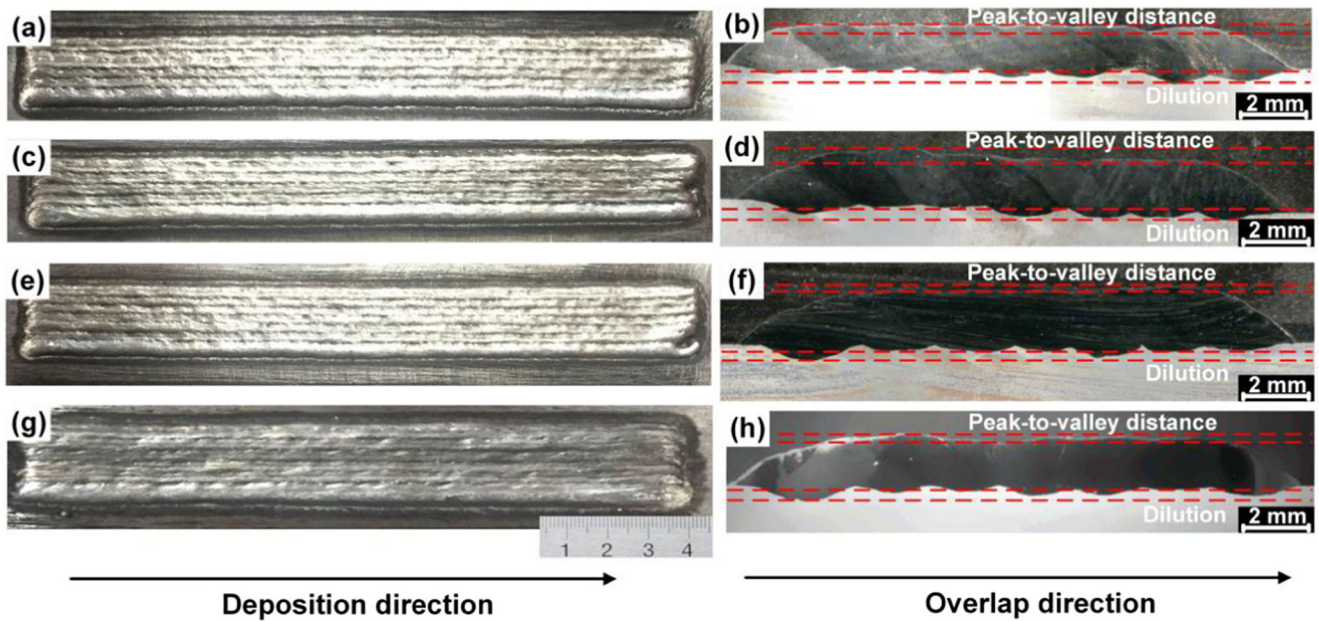


Fig. 12 The macroscopic appearance and cross section morphology of deposited layer: a, b condition A, S355; c, d condition D, S355; e, f condition E, S355; g, h condition D, AISI 420

Table 5 Geometry of the single layers

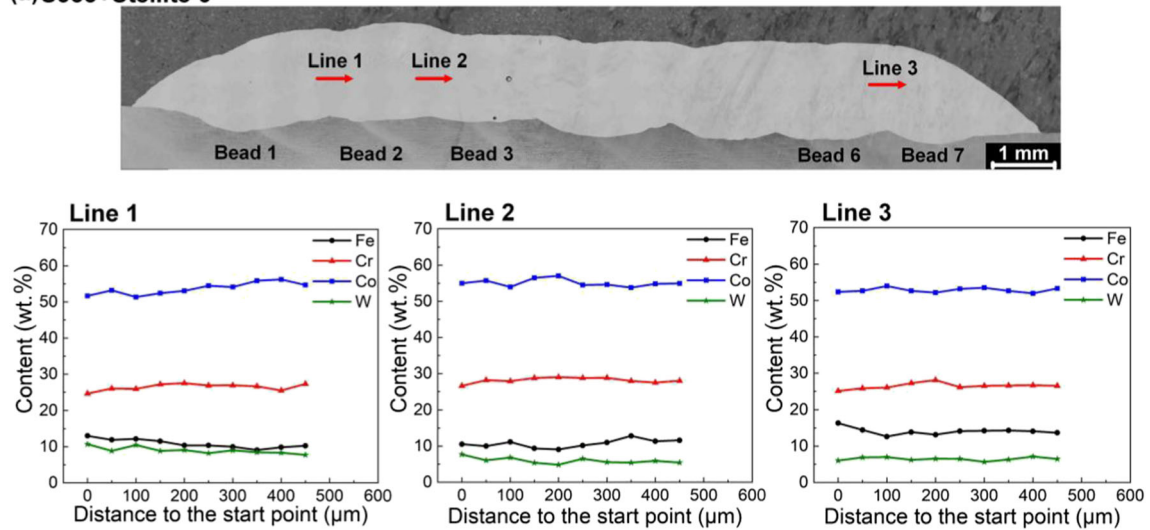
	Condition A (S355)	Condition D (S355)	Condition E (S355)	Condition D (AISI 420)
Energy input (J mm ⁻¹)	101	127	152	127
Surface waviness (μm)	400 ± 12	291 ± 8.7	150 ± 5.3	278 ± 7.3
Maximum dilution (%)	12.18 ± 0.25	18.05 ± 0.36	20.32 ± 0.44	19.6 ± 0.39
Minimum dilution (%)	7.89 ± 0.16	10.58 ± 0.21	15.08 ± 0.3	7.8 ± 0.16

layer in our study. These identified phases may contribute to the final corrosion, wear, and erosion properties of WAAM deposited Stellite 6, which will be the focus of our future research.

4 Conclusion

WAAM deposition of Stellite 6 on the different steel substrates was investigated in this study. It is concluded that

(a) S355+Stellite 6



(b) AISI 420+Stellite 6

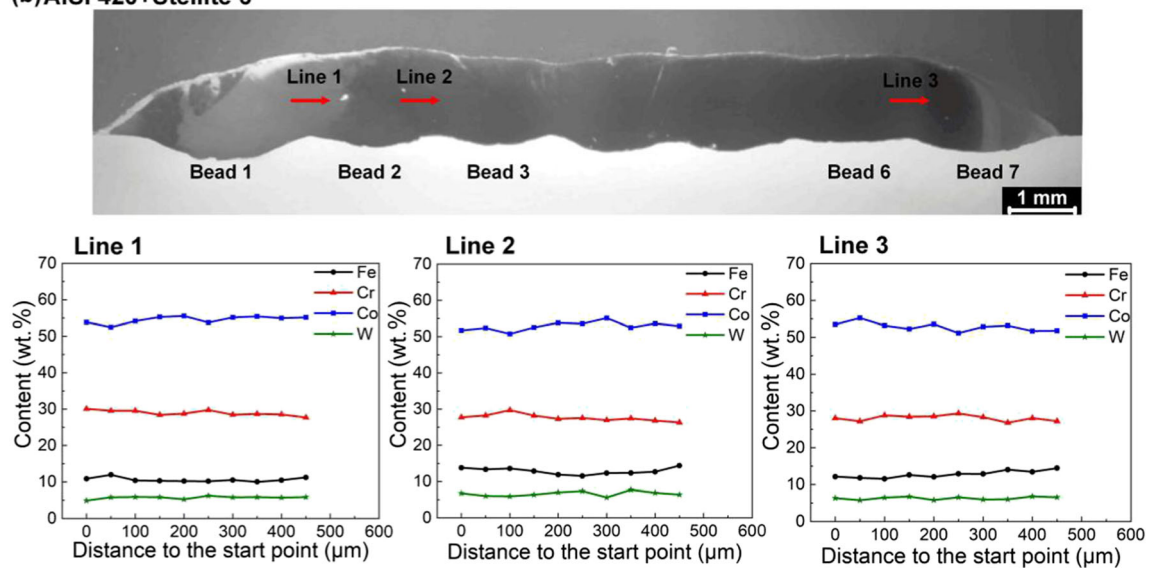


Fig. 13 EDS examination across the transverse cross section of the WAAM deposited Stellite 6 layer which measured across the adjacent overlapped beads: (a) on S355 steel substrate and (b) on AISI 420 steel substrate

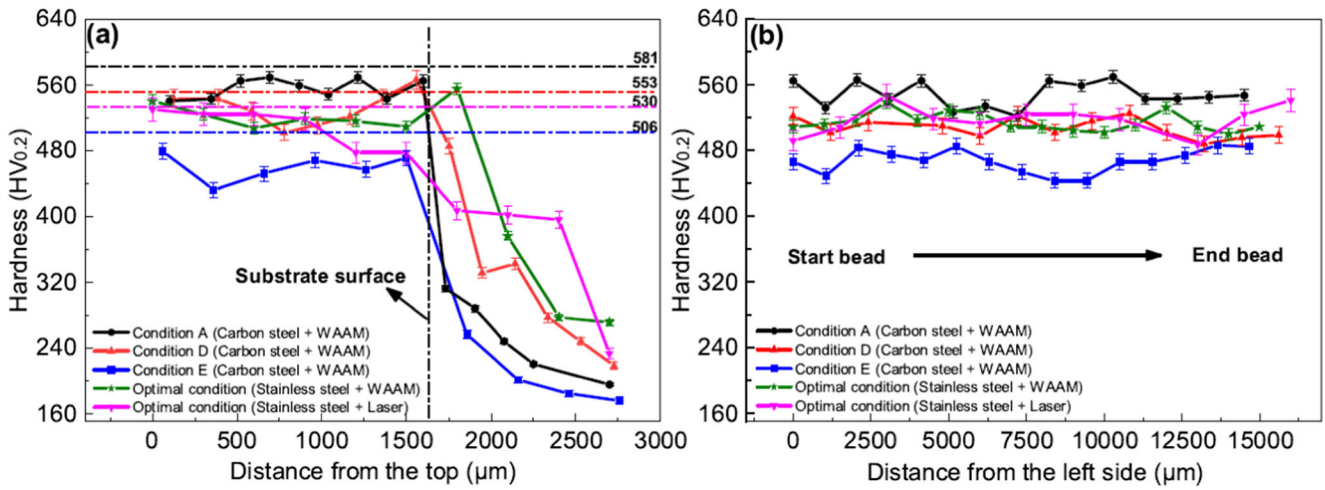
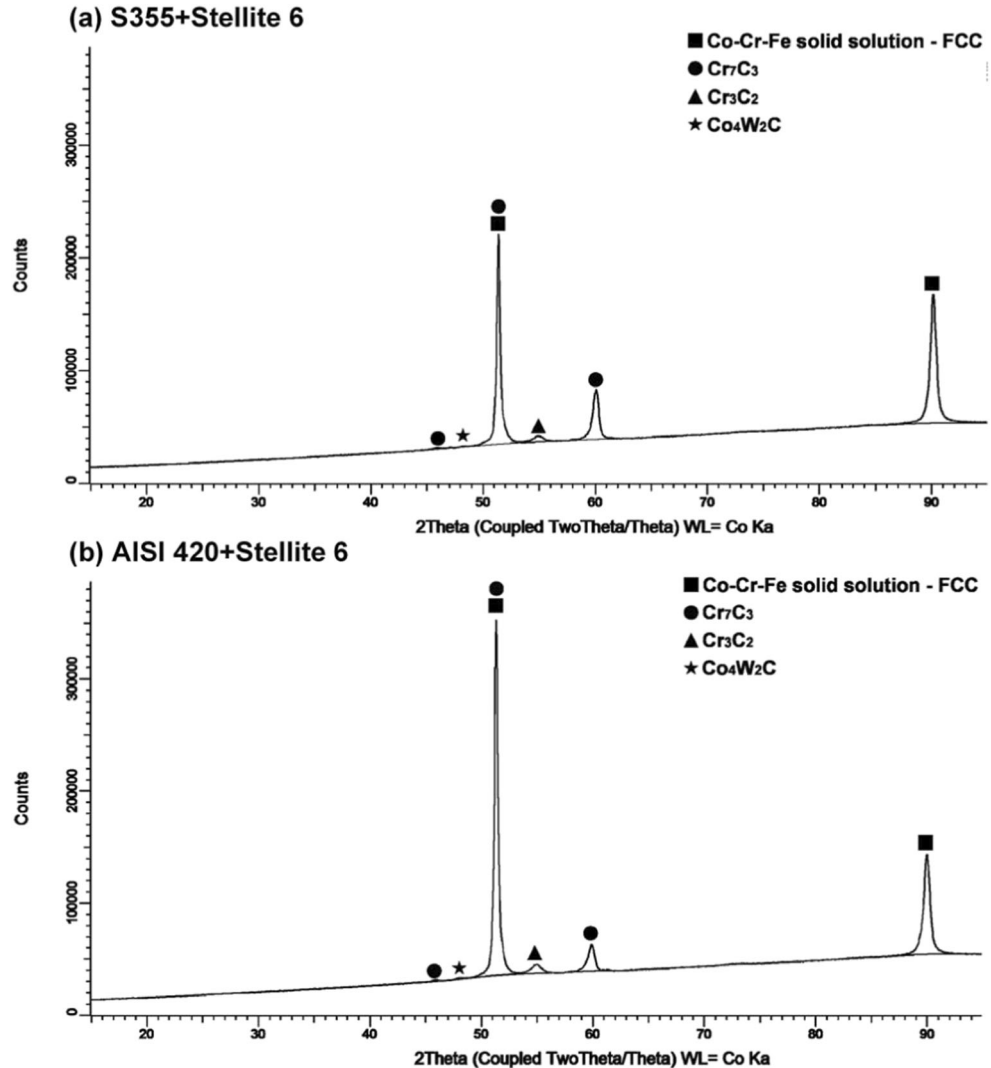


Fig. 14 Hardness measurements on middle of the single clad layer produced under different WAAM conditions: (a) across transverse section and (b) along longitudinal section

the same methodology was used for optimizing the laser cladding and can be used not only on the WAAM process

optimization of coating material but also on the different steel substrates.

Fig. 15 XRD phase identification of the WAAM deposited Stellite 6 on: (a) S355 + Stellite 6 and (b) AISI 420 + Stellite 6



With the optimized deposition parameters, a spreadable and continuous weld toe, little oxidation and silicide on the bead appearance, stable arc and melt droplet transfer during the process, and a near parabolic bead profile were realized. Defect-free Stellite 6 bead and layer mainly refers to the absence of crack and macropores in them. Stellite 6 beads and layers have been successfully deposited on both S355 and AISI 420 steel substrates with WAAM process.

A process window was established to guide the optimization of bead shape and dilution (geometrical). It was found in our study that a minimum heat input of 55 J mm^{-1} is needed to deposit a continuous bead. An increased heat input leads to grain growth and increased dilution, both of which contribute to the hardness reduction. The onset energy of Stellite 6 bead spreading is between 80 and 90 J mm^{-1} . A heat input of 127 J mm^{-1} was found to be optimal for depositing the Stellite 6 without jeopardizing its hardness while maintaining a good surface finishing. Considering the surface waviness and dilution, the optimal overlap ratio was found to be 42%. The deposition conditions optimized based on S355 steel substrate can be applied on the AISI 420 stainless steel substrate.

The results of hardness and EDS measurements, performed in transverse direction and in longitudinal direction of the deposited layer, show uniform values. This indicates that thermal cycle introduced during multi-beads deposition has limited effects on the material properties of deposited layer. The XRD analysis identified the presence of Co-Cr-Fe solid solution matrix with FCC crystal structure in the WAAM deposited Stellite 6 layer. The Cr_7C_3 and Cr_3C_2 carbides which can contribute to the strengthening mechanism and intermetallic compound with W ($\text{Co}_4\text{W}_2\text{C}$) which can contribute to the wear properties of the Stellite 6 WAAM deposits were also identified from the XRD and EDS analyses.

This research can provide a sound foundation for exploring the wear properties of the WAAM deposited Stellite 6 layer produced under various conditions. The multiple thermal cycles have limited effect on the microstructure, elemental distribution, relative uniform bonding, and hardness. In many industrial applications, WAAM can replace laser cladding as it is more economical, easy to adapt to robotic automation, and yields a high throughput.

Acknowledgments The authors would like to express sincere gratitude and thank all researchers from Delft University of Technology, University of Twente and RAMLAB who provided valuable supports and inputs to the project.

Funding This research was carried out under the master graduation project of the Delft University of Technology in collaboration with the Rotterdam Fieldlab Additive Manufacturing BV. (RAMLAB). Dr. Constantinos Goulas was funded by the Dutch organization for scientific research (NWO-Nederlandse Organisatie voor Wetenschappelijk Onderzoek) in the framework of project GradWAAM, Project Number S16043. A special thanks to Mr. Vincent Wegener, Managing Director, RAMLAB to provide financial support for this project.

References

1. Yangtao X, Tiandong X, Yanling H (2009) Microstructures comparison of Stellite 6 alloy by self-propagating high-temperature synthesis and cast HS111 alloy. *Rare Metal Mater Eng* 38(8): 1333–1337
2. Derow H., & Bleil HE (1970) *Elevated temperature instability of Stellite 6B* (Vol. 1590). National Aeronautics and Space Administration.
3. Zangeneh S, Farhangi H (2010) Influence of service-induced microstructural changes on the failure of a cobalt-based superalloy first stage nozzle. *Mater Des* 31(7):3504–3511
4. Marques FP, Scandian C, Bozzi AC, Fukumasu NK, Tschiptschin AP (2017) Formation of a nanocrystalline recrystallized layer during microabrasive wear of a cobalt-chromium based alloy (Co-30Cr-19Fe). *Tribol Int* 116:105–112
5. Rebouças Filho PP, da Silveira Cavalcante T, de Albuquerque VHC, Tavares JMR, & Cortez PC (2009) Measurement of welding dilution from images using active contours. In *SEECCM 2009-2nd South-East European Conference on Computational Mechanics*.
6. Kuzucu V, Ceylan M, Celik H, Aksoy I (1997) Microstructure and phase analyses of Stellite 6 plus 6 wt.% Mo alloy. *J Mater Process Technol* 69(1-3):257–263
7. Ya W, Pathiraj B, Matthews DT, Bright M, Melzer S (2018) Cladding of Tribaloy T400 on steel substrates using a high power Nd: YAG laser. *Surf Coat Technol* 350:323–333
8. Gholipour A, Shamanian M, Ashrafizadeh F (2011) Microstructure and wear behavior of stellite 6 cladding on 17-4 PH stainless steel. *J Alloys Compd* 509(14):4905–4909
9. Malayoglu U, Neville A, Lovelock H (2005) Assessing the kinetics and mechanisms of corrosion of cast and HIPed Stellite 6 in aqueous saline environments. *Corros Sci* 47(8):1911–1931
10. Sidhu TS, Prakash S, Agrawal RD (2006) Studies of the metallurgical and mechanical properties of high velocity oxy-fuel sprayed stellite-6 coatings on Ni- and Fe-based superalloys. *Surf Coat Technol* 201(1-2):273–281
11. Opris CD, Liu R, Yao MX, Wu XJ (2007) Development of Stellite alloy composites with sintering/HIPing technique for wear-resistant applications. *Mater Des* 28(2):581–591
12. Sidhu BS, Puri D, Prakash S (2005) Mechanical and metallurgical properties of plasma sprayed and laser remelted Ni–20Cr and Stellite-6 coatings. *J Mater Process Technol* 159(3):347–355
13. Ya W, Pathiraj B (2018) Residual stresses in Stellite 6 layers clad on AISI 420 steel plates with a Nd: YAG laser. *J Laser Appl* 30(3):032007
14. Ya, W. (2015). Laser materials interactions during cladding: analyses on clad formation, thermal cycles, residual stress and defects.
15. Heralić A, Christiansson AK, Ottosson M, Lennartson B (2010) Increased stability in laser metal wire deposition through feedback from optical measurements. *Opt Lasers Eng* 48(4):478–485
16. Sun S, Durandet Y, Brandt M (2005) Parametric investigation of pulsed Nd: YAG laser cladding of stellite 6 on stainless steel. *Surf Coat Technol* 194(2-3):225–231
17. Brandt M, Sun S, Alam N, Bendeich P, Bishop A (2009) Laser cladding repair of turbine blades in power plants: from research to commercialisation. *Int Heat Treat Surf Eng* 3(3):105–114
18. Piasecki ADAM, Bartkowski DARIUSZ, Młynarczyk A, Dudziak A, Gościński M, Kasproviak MONIKA (2013) Laser cladding of Stellite 6 on low carbon steel for repairing components in automotive applications using disk laser. *Arch Mech Technol Autom* 33(2):25–34
19. Sarafan S, Wanjara P, Champlaud H, Thibault D (2015) Characteristics of an autogenous single pass electron beam weld in thick gage CA6NM steel. *Int J Adv Manuf Technol* 78(9-12): 1523–1535

20. Hemmati, I., Ocelík, V., & De Hosson, J. T. M. (2015). Compositional modification of Ni-base alloys for laser-deposition technologies. In *Laser Surface Engineering* (pp. 137–162). Woodhead Publishing.
21. Ya W, & Hamilton K (2017) On-demand spare parts for the marine industry with directed energy deposition: propeller use case. In *International Conference on Additive Manufacturing in Products and Applications* (pp. 70–81). Springer, Cham.
22. Sarathchandra DT, Davidson MJ, Visvanathan G (2020) Parameters effect on SS304 beads deposited by wire arc additive manufacturing. *Mater Manuf Process* 35(7):852–858
23. Li Z, Cui Y, Wang J, Liu C, Wang J, Xu T et al (2019) Characterization of microstructure and mechanical properties of Stellite 6 part fabricated by wire arc additive manufacturing. *Metals* 9(4):474
24. Busachi A, Erkoyuncu J, Colegrove P, Martina F, Watts C, Drake R (2017) A review of additive manufacturing technology and cost estimation techniques for the defence sector. *CIRP J Manuf Sci Technol* 19:117–128
25. Williams SW, Martina F, Addison AC, Ding J, Pardal G, Colegrove P (2016) Wire+ arc additive manufacturing. *Mater Sci Technol* 32(7):641–647
26. Murr LE, Gaytan SM, Ceylan A, Martinez E, Martinez JL, Hernandez DH et al (2010) Characterization of titanium aluminide alloy components fabricated by additive manufacturing using electron beam melting. *Acta Mater* 58(5):1887–1894
27. Kim TB, Yue S, Zhang Z, Jones E, Jones JR, Lee PD (2014) Additive manufactured porous titanium structures: through-process quantification of pore and strut networks. *J Mater Process Technol* 214(11):2706–2715
28. Gardner L, Kyvelou P, Herbert G, Buchanan C (2020) Testing and initial verification of the world's first metal 3D printed bridge. *J Constr Steel Res* 172:106233
29. Lange J, Feucht T, Erven M (2020) 3D printing with steel: additive Manufacturing for connections and structures. *Steel Construction* 13(3):144–153
30. Laghi V, Palermo M, Gasparini G, & Trombetti T (2020) Computational design and manufacturing of a half-scaled 3D-printed stainless steel diaphragm column. *Addit Manuf*, 101505.
31. Meboldt M, Klahn C. (Eds.). (2017) *Industrializing additive manufacturing-proceedings of additive manufacturing in products and applications-AMPA2017*. Springer
32. Bahrin MAK, Othman MF, Azli NHN, & Talib MF (2016) Industry 4.0: a review on industrial automation and robotic. *Jurnal Teknologi*, 78(6-13).
33. Martina F, Ding J, Williams S, Caballero A, Pardal G, Quintino L (2019) Tandem metal inert gas process for high productivity wire arc additive manufacturing in stainless steel. *Addit Manuf* 25:545–550
34. Pickin CG, Young K, Tuersley I (2007) Joining of lightweight sandwich sheets to aluminium using self-pierce riveting. *Mater Des* 28(8):2361–2365
35. Watanabe T, Takayama H, Yanagisawa A (2006) Joining of aluminium alloy to steel by friction stir welding. *J Mater Process Technol* 178(1-3):342–349
36. McCaw RL (1979) *Plasma ARC welding of high-performance-ship materials*. David W Taylor Naval ship research and development center annapolis md ship materials engineering dept.
37. Muncaster PW (1991) *A practical guide to TIG (GTA) welding*. Elsevier
38. Sweet LM (1985) Sensor-based control systems for arc welding robots. *Robot Comput Integr Manuf* 2(2):125–133
39. Bhagi LK, Gupta P, Rastogi V (2013) Fractographic investigations of the failure of L-1 low pressure steam turbine blade. *case studies in. Eng Fail Anal* 1(2):72–78
40. Ahmad M, Schatz M, Casey MV (2013) Experimental investigation of droplet size influence on low pressure steam turbine blade erosion. *Wear* 303(1-2):83–86
41. Ya W, Pathiraj B, Liu S (2016) 2D modelling of clad geometry and resulting thermal cycles during laser cladding. *J Mater Process Technol* 230:217–232
42. Ya W, Hernández-Sánchez JF, Pathiraj B, & Veld AHIT (2013) A study on attenuation of a Nd: YAG laser power by co-axial and off-axial nozzle powder stream during cladding. In *International Congress on Applications of Lasers & Electro-Optics* (Vol. 2013, No. 1, pp. 453–462). Laser Institute of America.
43. Dinovitzer M, Chen X, Laliberte J, Huang X, Frei H (2019) Effect of wire and arc additive manufacturing (WAAM) process parameters on bead geometry and microstructure. *Addit Manuf* 26:138–146
44. Abe T, Sasahara H (2019) Layer geometry control for the fabrication of lattice structures by wire and arc additive manufacturing. *Addit Manuf* 28:639–648
45. de Oliveira UOB (2007) *Laser treatment of alloys: processing, microstructure and structural properties*. University Library Groningen[[Host].
46. Lin Z, Goulas C, Ya W, Hermans MJ (2019) Microstructure and mechanical properties of medium carbon steel deposits obtained via wire and arc additive manufacturing using metal-cored wire. *Metals* 9(6):673
47. Hashmi S (2014) *Comprehensive materials processing*. Newnes
48. Schneider MF, & Schneider MF (1998) Laser cladding with powder.
49. Webb CE, & Jones JD (Eds.). (2004) *Handbook of laser technology and applications: laser design and laser systems* (Vol. 2). CRC Press
50. DuPont JN, Marder AR (1995) Thermal efficiency of arc welding processes. *Welding Journal-Including Welding Research Supplement* 74(12):406 s
51. Kumar S, Shahi AS (2011) Effect of heat input on the microstructure and mechanical properties of gas tungsten arc welded AISI 304 stainless steel joints. *Mater Des* 32(6):3617–3623
52. Khromchenko FA, Lappa VA, Fedina IV, Karev AN, Dolzhanskii PR (1999) Technology of repairing working blades of steam turbines. Part 1. Repair by the method of deposition of high-Cr alloys. *Weld Int* 13(5):405–408
53. Ferozhkhan MM, Duraiselvam M, Ravibharath R (2016) Plasma transferred arc welding of Stellite 6 alloy on stainless steel for wear resistance. *Procedia Technology* 25:1305–1311
54. Kusmoko A, Dunne DP, Li H, & Nolan DJ (2013) Deposition of Stellite 6 on nickel superalloy and mild steel substrates with laser cladding
55. Yan F, Xiong W, Faierson EJ (2017) Grain structure control of additively manufactured metallic materials. *Materials* 10(11):1260
56. Houdková ěárka, Pala Z, Smazalová Eva, Vostřák, Marek, & ěesánek, Zdeněk. (2016) Microstructure and sliding wear properties of hvof sprayed, laser remelted and laser clad stellite 6 coatings. *Surface and Coatings Technology*, S0257897216308817.
57. Xu G, Kutsuna M, Liu Z, Yamada K (2006) Comparison between diode laser and tig cladding of co-based alloys on the sus403 stainless steel. *Surf Coat Technol* 201(3-4):1138–1144
58. Silwal B, Walker J, West D (2019) Hot-wire GTAW cladding: inconel 625 on 347 stainless steel. *Int J Adv Manuf Technol* 102(9-12):3839–3848
59. Valsecchi B, Previtali B, Gariboldi E (2012) Fibre laser cladding of turbine blade leading edges: the effect of specific energy on clad dilution. *Int J Struct Integ* 3(4):377–395

Publisher's note Springer Nature remains neutral with regard to jurisdictional claims in published maps and institutional affiliations.